Supplementary Information

Thermally-stable threshold selector based on CuAg alloy for energy-efficient memory and neuromorphic computing applications

Xi Zhou, Liang Zhao*, Chu Yan, Weili Zhen, Yinyue Lin, Le Li, Guanlin Du, Linfeng Lu, Shan-Ting Zhang, Zhichao Lu, Dongdong Li*

*email: lzhao2020@zju.edu.cn, lidd@sari.ac.cn

This file includes:

Supplementary Figures 1-11

Supplementary Tables 1-2

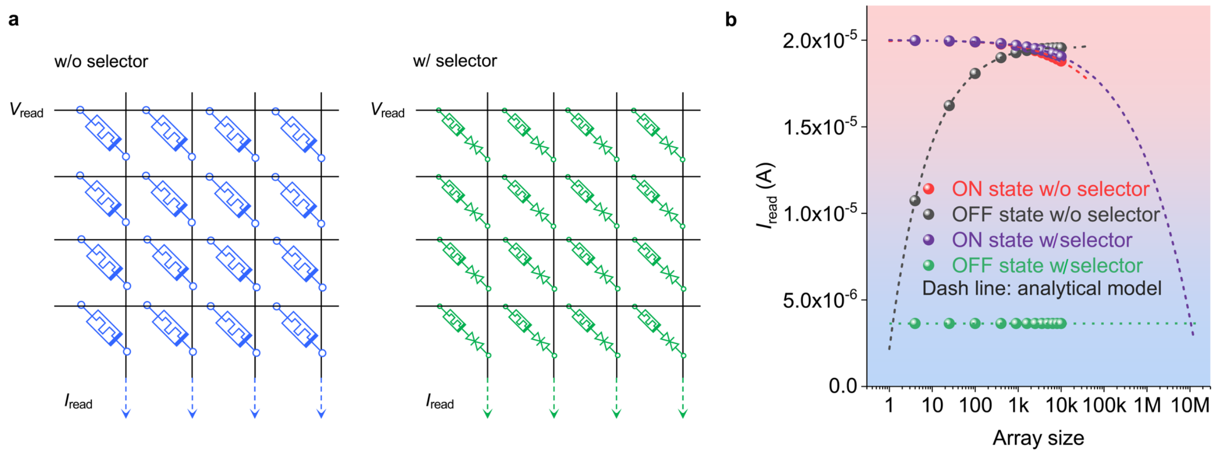

Supplementary Figure 1. a, Schematic diagram of the worst-case read current (I_{read}) of the cross-point array simulated using SPICE (see Methods). The worst-case of the ON state is to read the cell that is farthest from the power line, and then the other cells are OFF, and the worst-case of the OFF state is to read the cell that is closest to the power line, and the other cells are ON. **b**, I_{read} variation with array size with and without selector, where the spheres indicate the results of simulations using SPICE and the dashed lines indicate the results of simulations using the analytical model. The simulation parameters are shown in Supplementary Table **1**. Without the selector, it is no longer possible to perform a correct read operation the array size reaches 10 (worst case ON/OFF ratio<2), while the case with the selector is able to allow a larger integration (>1 M) and operation window.

Supplementary Table 1. Device parameters for the simulation process include read voltage (V_{read}), ON and OFF state resistance (R_{ON} and R_{OFF}) and series resistance (R_{sr}).

Parameter name	Value
R_{ON}	10000 Ω
R_{OFF} (w/o selector)	200000 Ω
R_{OFF} (w/ selector)	10^{11} Ω
R_{sr} (between cells)	5 Ω
R_{sr} (output terminal)	100 Ω
V_{read}	0.4 V

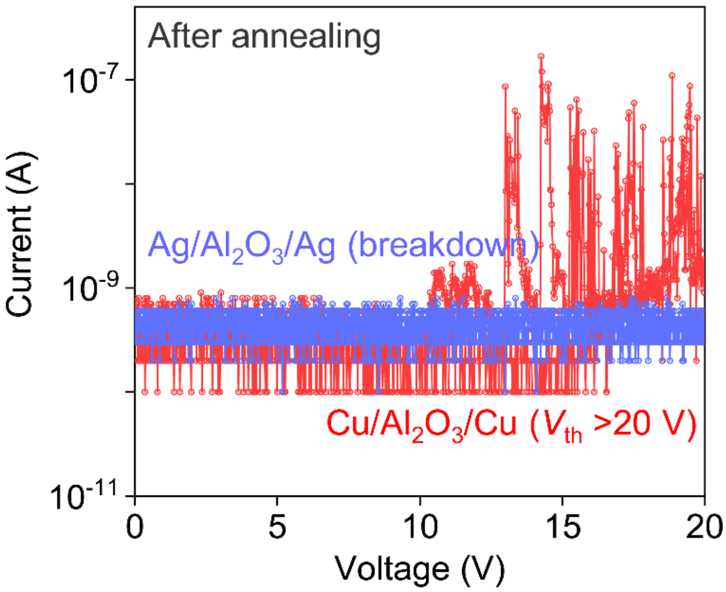

Supplementary Figure 2. Current–voltage (*I*–*V*) characteristics of annealed Ag/Al_2O_3/Ag and Cu/Al_2O_3/Cu selectors (400 ºC, Ar atmosphere, 1 hour).

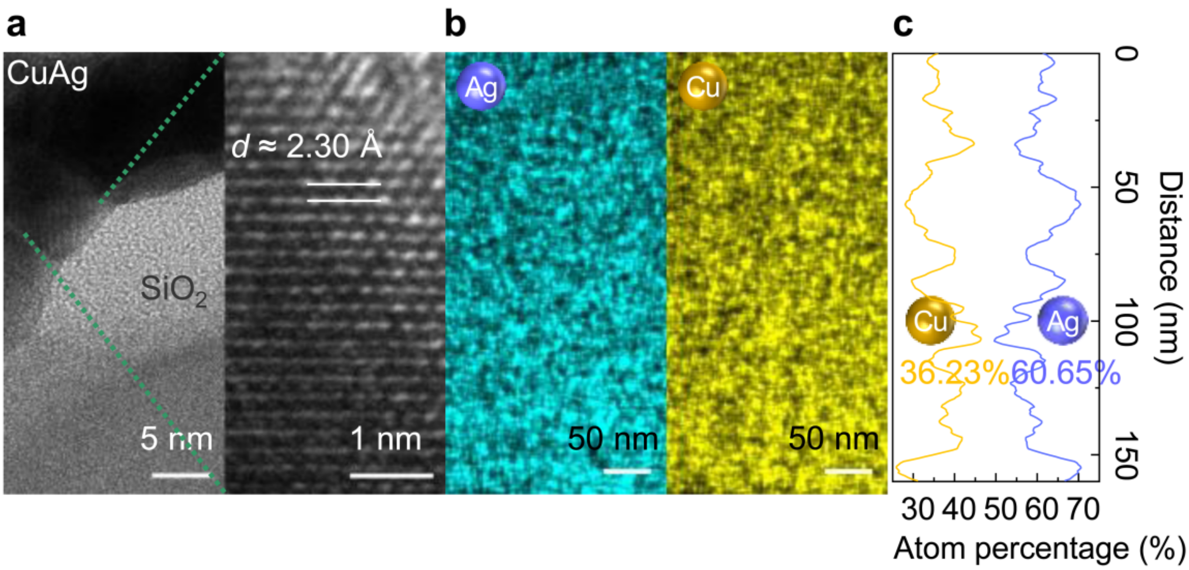

Supplementary Figure 3. a, STEM image of the CuAg electrode. The lattice fringe with an interplanar spacing (*d*) of 2.30 Å is attributed to the CuAg alloy (111) plane, which is consistent with XRD results (Fig. 1**f**). As for XRD results, The (111) interplanar spacings (d_{111}) of Ag, Cu and CuAg, calculated by the Bragg's Law[1] from XRD patterns, are 2.35, 2.08 and 2.30 Å, respectively. **b**, The EDS mapping and (**c**) linear sweep results for Ag and Cu elements in CuAg electrode. The mean values of the atomic percentages of Ag and Cu are 60.65% and 36.23%, corresponding to an atomic ratio of about 5:3. The higher Ag content supports why the d_{111} of the CuAg alloy is closer to that of Ag. The CuAg prepared by co-sputtering is determined by XRD as a nanocrystalline alloy (Fig. 1**f**). The diffraction peak at 39.06^{o} is significantly broadened with a full width at half maximum (~1.34^{o}). The corresponding crystalline size (*D*) is estimated to be ~6.29 nm acquired by Debye-Scherrer equation[2].

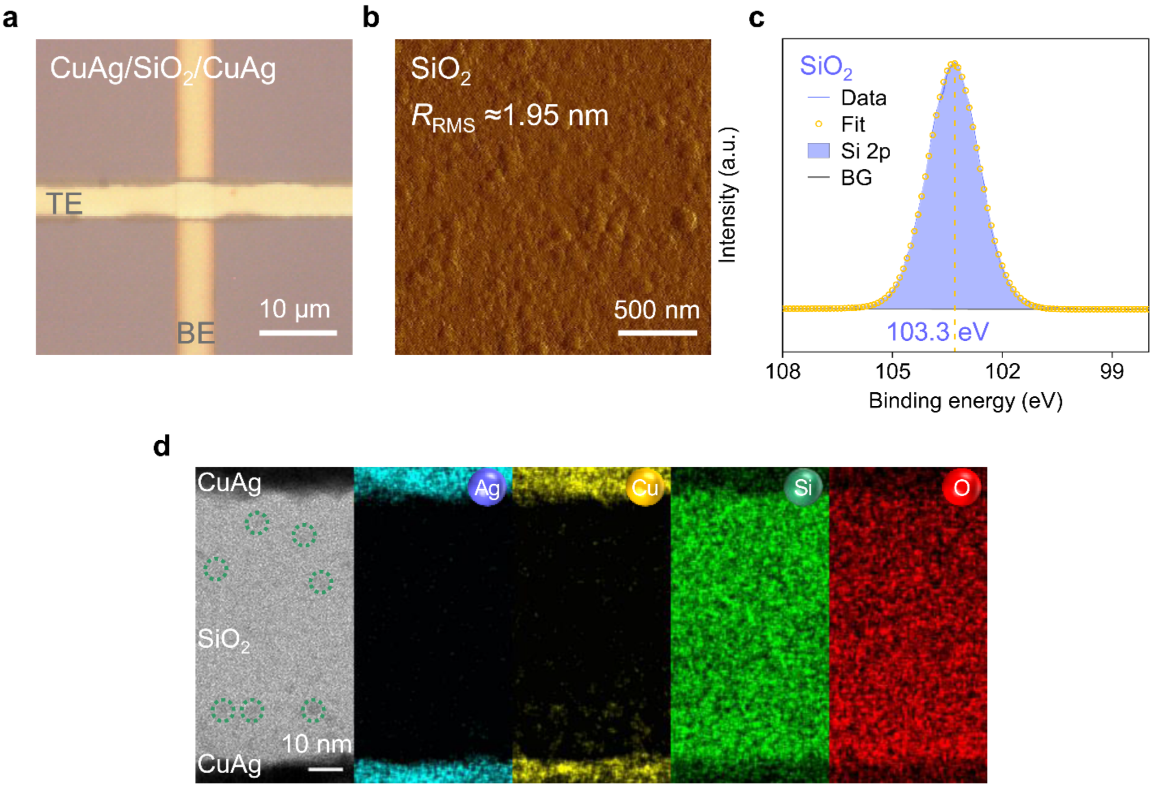

Supplementary Figure 4. Structure of the CuAg/SiO_2/CuAg selector and some basic properties of the SiO_2 interlayer. **a**, A top view of CuAg/SiO_2/CuAg selector, the electrode linewidths of bottom electrode (BE) and top electrode (TE) are 5 μm. Since the SiO_2 layer and the TE are patterned together, the SiO_2 cannot be directly observed. **b**, AFM image of the SiO_2 film. **c**, XPS spectrum of the SiO_2 film. **d**, Cross-sectional STEM image of the CuAg/SiO_2/CuAg selector and corresponding EDS elemental mapping of Ag, Cu, Si, and O. The green circles mark the diffused Cu and Ag particles, which appear spherical due to minimized interfacial energy[3].

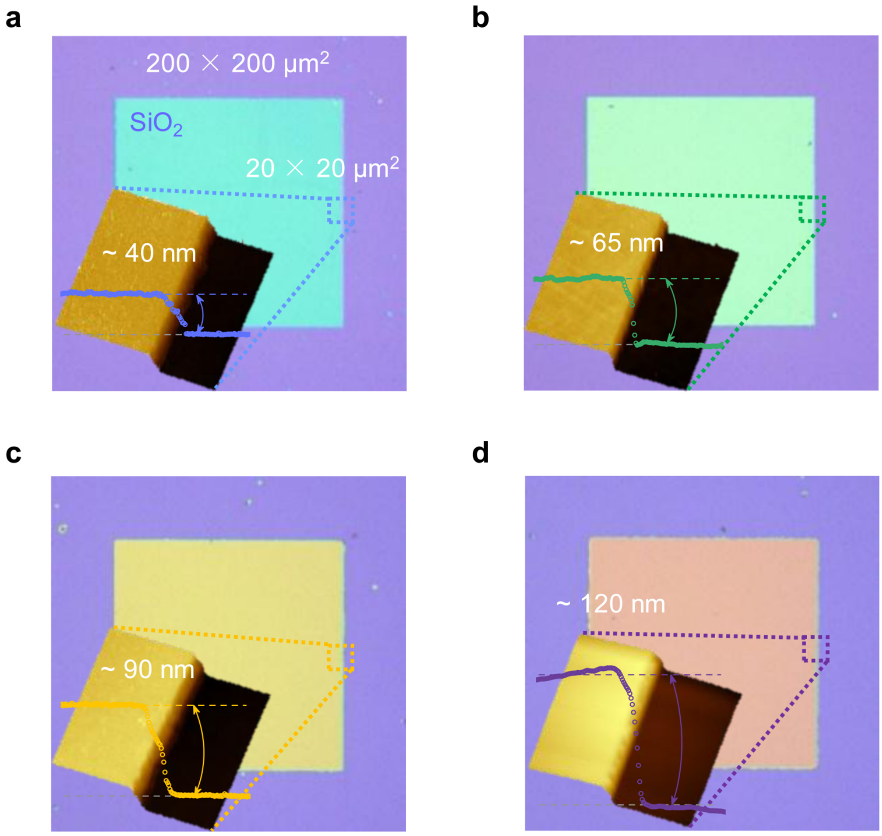

Supplementary Figure 5. Calibration of the thickness of the SiO_2 interlayers for CuAg/SiO_2/CuAg selectors. The SiO_2 interlayers are patterned and tested using AFM to obtain their thicknesses of (**a**) 40, (**b**) 65, (**c**) 90, and (**d**) 120 nm, respectively.

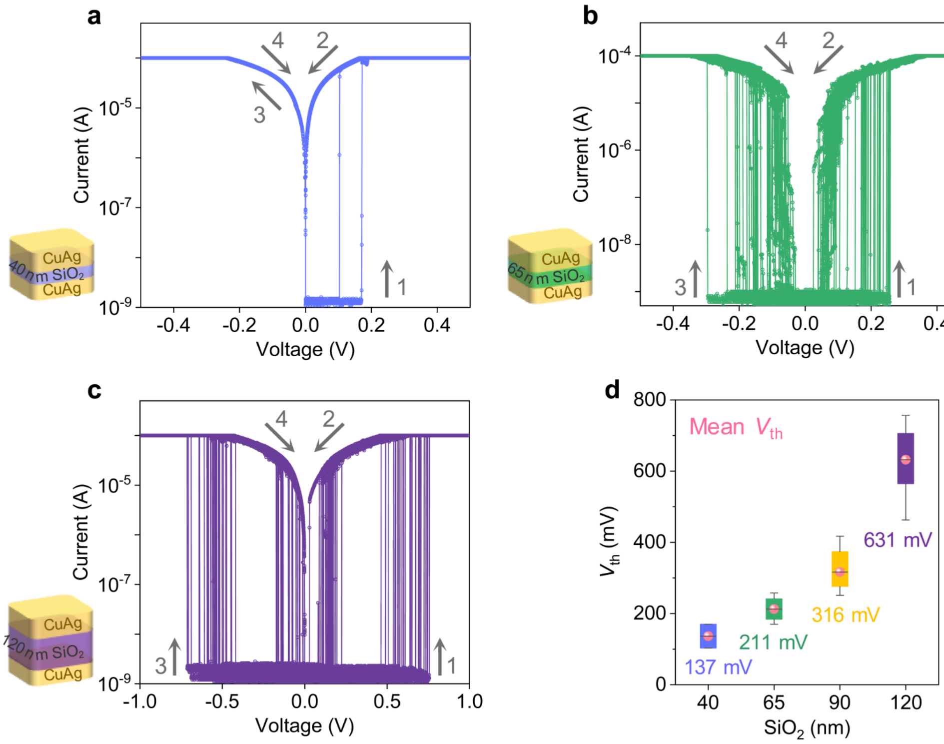

Supplementary Figure 6. Adjustable threshold voltage (V_{th}) achieved by varying the thickness of the SiO_2 dielectrics. *I*–*V* characteristics of (**a**) CuAg/40 nm SiO_2/CuAg, (**b**) CuAg/65 nm SiO_2/CuAg and (**c**) CuAg/120 nm SiO_2/CuAg selectors. **d**, Variation of the V_{th} with the thickness of SiO_2 interlayer. For selectors with 40 nm SiO_2, it is difficult to maintain the symmetric threshold switching characteristic as they remain in the ON state after the first turn-on and are difficult to return to the OFF state (**a**) probably due to the presence of pin-holes. While the devices with 65 nm SiO_2 demonstrate the complete ON/OFF switching process with an average V_{th} of 211 mV (**b**,**d**). Devices with a SiO_2 interlayer thickness of 120 nm have a higher average V_{th} of 631 mV (**c**,**d**). These results confirm that the V_{th} of proposed selectors can be tuned by adjusting the interlayer thickness.

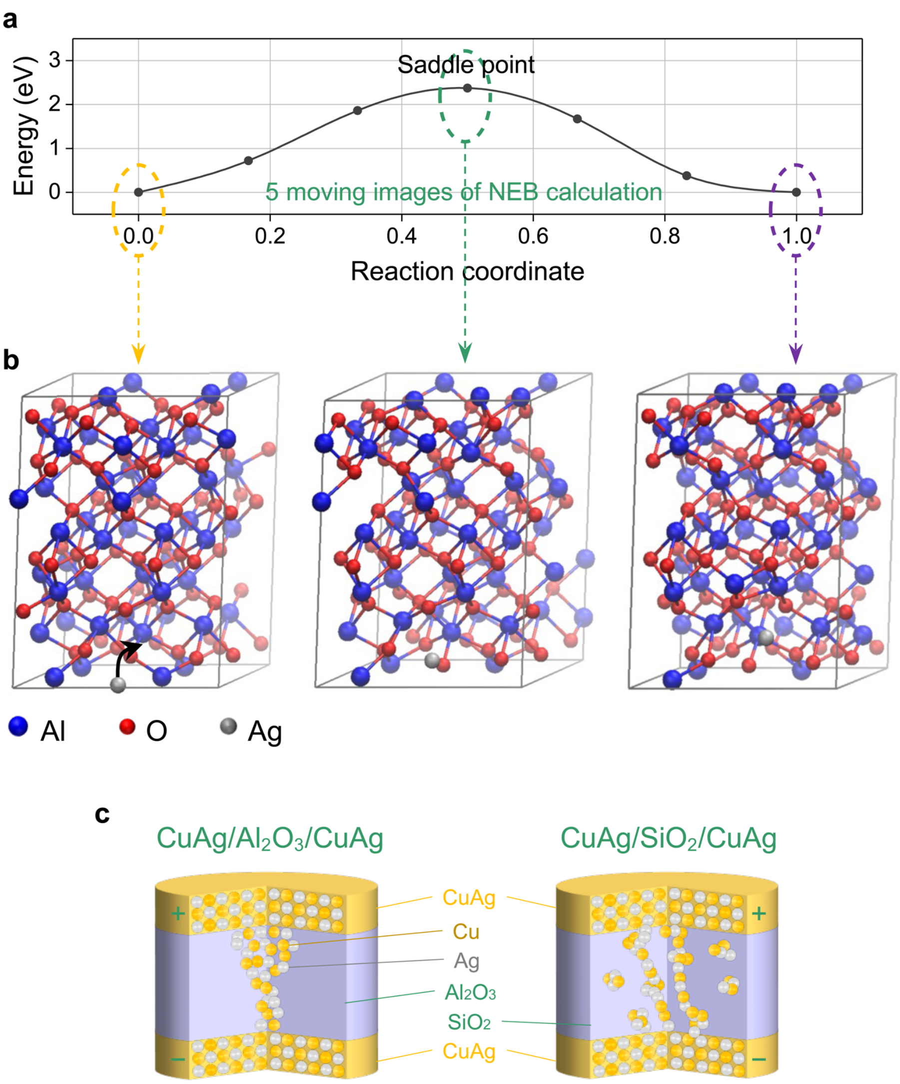

Supplementary Figure 7. a, Energy profile of Ag migration in Al_2O_3, calculated by density functional theory (DFT) and the nudged-elastic-band (NEB) method. The simulated system comprises of a supercell of trigonal Al_2O_3 ($R\bar{3}c$ space group) with 48 Al atoms and 72 O atoms. The DFT simulations are carried out based on the projector augmented-wave (PAW) method[4,5] and the general-gradient approximation (GGA) with Perdew–Burke–Ernzerhof (PBE)[6] pseudopotentials, as implemented by the Vienna Ab initio Simulation Package (VASP)[7–10]. The initial and final configurations with one additional Ag atom introduced as an interstitial are fully relaxed to obtain the ground state, with electronic relaxation converged to 1×10^{-8} eV/atom and interatomic forces smaller than 1×10^{-4} eV/Å. The relaxed unit cells are then used to construct the NEB calculations with the climbing image method (CI-NEB)[11–13], which allows more accurate finding of saddle points with fewer images (5 images in this case). Multiple potential migration paths are calculated and the one with lowest energy is plotted. **b**, The Al_2O_3 supercell structures along the Ag migration path corresponding to the migration barrier in (**a**), relaxed with the CI-NEB. The Supplementary Table **2** summarizes the migration barriers and Bader charges for Ag/Ag^+ in SiO_2, ZrO_2 and Al_2O_3. The results for SiO_2 and ZrO_2 are adapted from the ref. [14]. In ZrO_2, because the Bader charges of Ag and Ag^+ are 0.57 *e* and 0.58 *e*, and the valence state of Zr is variable, thus the Ag interstitial always stays as a cation[14]. In SiO_2 and Al_2O_3, the Bader charges of Ag (0.16 *e* and 0.066 *e*) are substantially lower than Ag^+ (0.72 *e* and 0.327 *e*), thus there are two states (Ag and Ag^+) for the silver interstitial. On the other hand, the migration barrier results show that the barrier of Ag and Ag^+ in Al_2O_3 (2.37 eV and 3.47 eV) is much larger than that in SiO_2 (0.61 eV and 0.53 eV), indicating that the formation of conductive filaments in SiO_2 is easier. In general, the Ag^+ in ZrO_2 migrates continuously with the electric field and is easy to form non-volatile memristors[15]. The presence of both Ag and Ag^+ in Al_2O_3 and SiO_2 makes it easy to form volatile selectors through clustering. At the same time, the migration barrier of silver in SiO_2 is much lower, thus the switching speed is faster and it is easier to form electroforming-free devices. Combined with the results of STEM (Fig. S4**d**), metals exist in the form of clusters in SiO_2. When a bias voltage is applied, the clusters on the anode side release metals, and the clusters on the cathode side accumulate metals until conductive filaments are formed connecting both terminals. When the applied voltage is less than the hold voltage, the metal in the filament migrates back into the clusters or electrodes due to the very low migration barrier in SiO_2, enabling volatile resistance switching. **c**, Schematic diagram of the conductive filament morphology of CuAg/Al_2O_3/CuAg and CuAg/SiO_2/CuAg selectors in the ON state. For the CuAg/Al_2O_3/CuAg selector, even though the migration barrier of metal atoms in Al_2O_3 is large, conical conductive filaments can still be formed in the ultrathin Al_2O_3 film. For the CuAg/SiO_2/CuAg selector, due to the small migration barrier of the metal, in the ON state, the metal in the electrodes and clusters form connected conductive filaments.

Supplementary Table 2. The migration barriers and Bader charges for Ag/Ag^+ in SiO_2, ZrO_2 and Al_2O_3. The results for SiO_2 and ZrO_2 are adapted from the ref. [14].

Dielectrics	Migration barrier (eV)		Bader charges	
	Ag	Ag^+	Ag (*e*)	Ag^+ (*e*)
SiO_2	0.61	0.53	0.16	0.72
ZrO_2	2.39	2.48	0.57	0.58
Al_2O_3	2.37	3.47	0.066	0.327

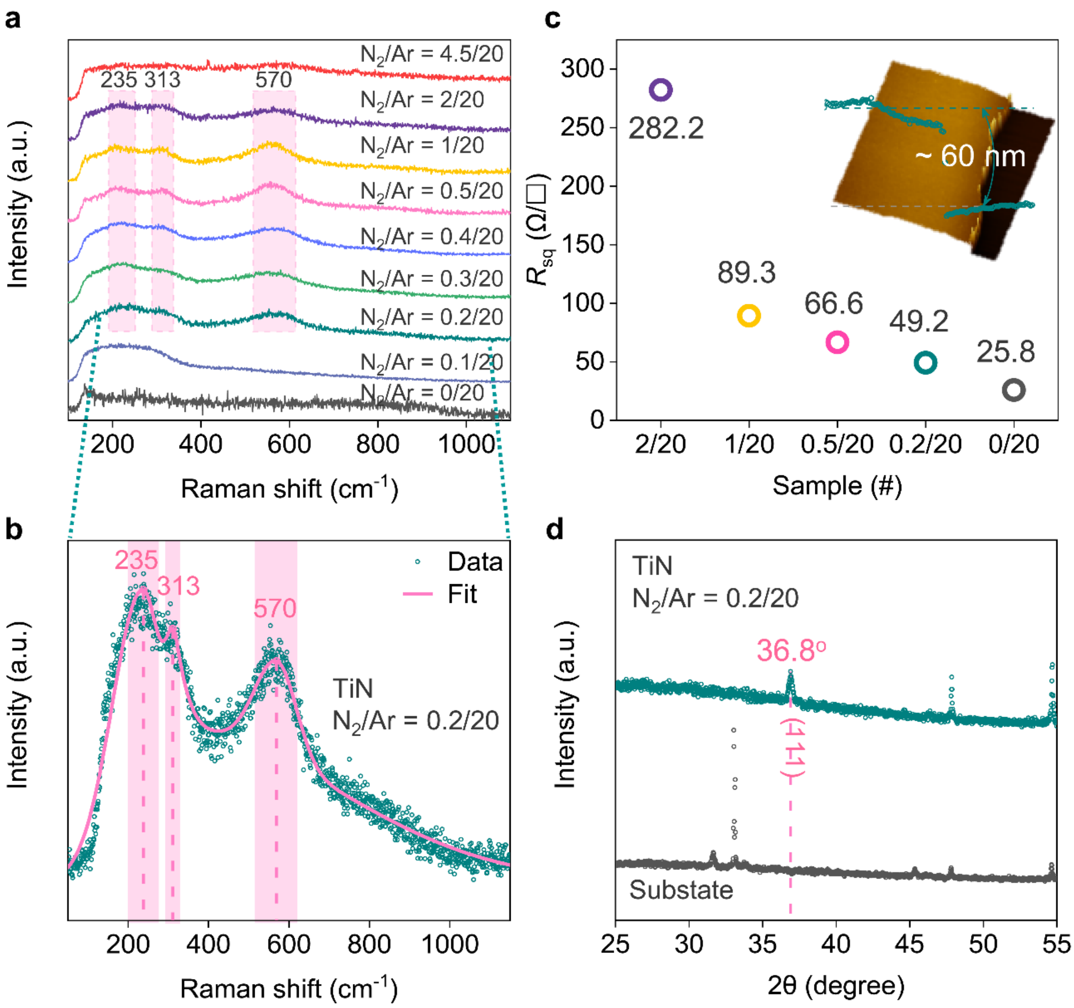

Supplementary Figure 8. Basic characteristics about the TiN electrodes. a, Raman spectra of the films prepared by sputtering Ti target in different N_2/Ar flow ratios at room temperature. Controlling the N_2/Ar flow ratio between 0.2/20 and 2/20 enables the TiN films to be obtained. **b**, A close view of Raman spectrum of the TiN film with a N_2/Ar flow ratio of 0.2/20. A series peaks (235, 313, 570 cm^{-1}) corresponding to the characteristic vibration modes of TiN[16]. **c,** Square resistance (R_{sq}) of the TiN films deposited at various N_2/Ar flow ratio. The square resistance of the TiN films decreases as the nitrogen concentration decreases[17]. The thickness of the TiN TE used in the Pt/SiO_2/TiN memristor is ~60 nm with the R_{sq} of ~49.2 Ω/□ (N_2/Ar flow ratio = 0.2/20). **d**, XRD patterns of the SiO_2/Si substrate and TiN film (N_2/Ar flow ratio = 0.2/20). The peak at 36.80° corresponds to the (111) crystal plane of TiN[18].

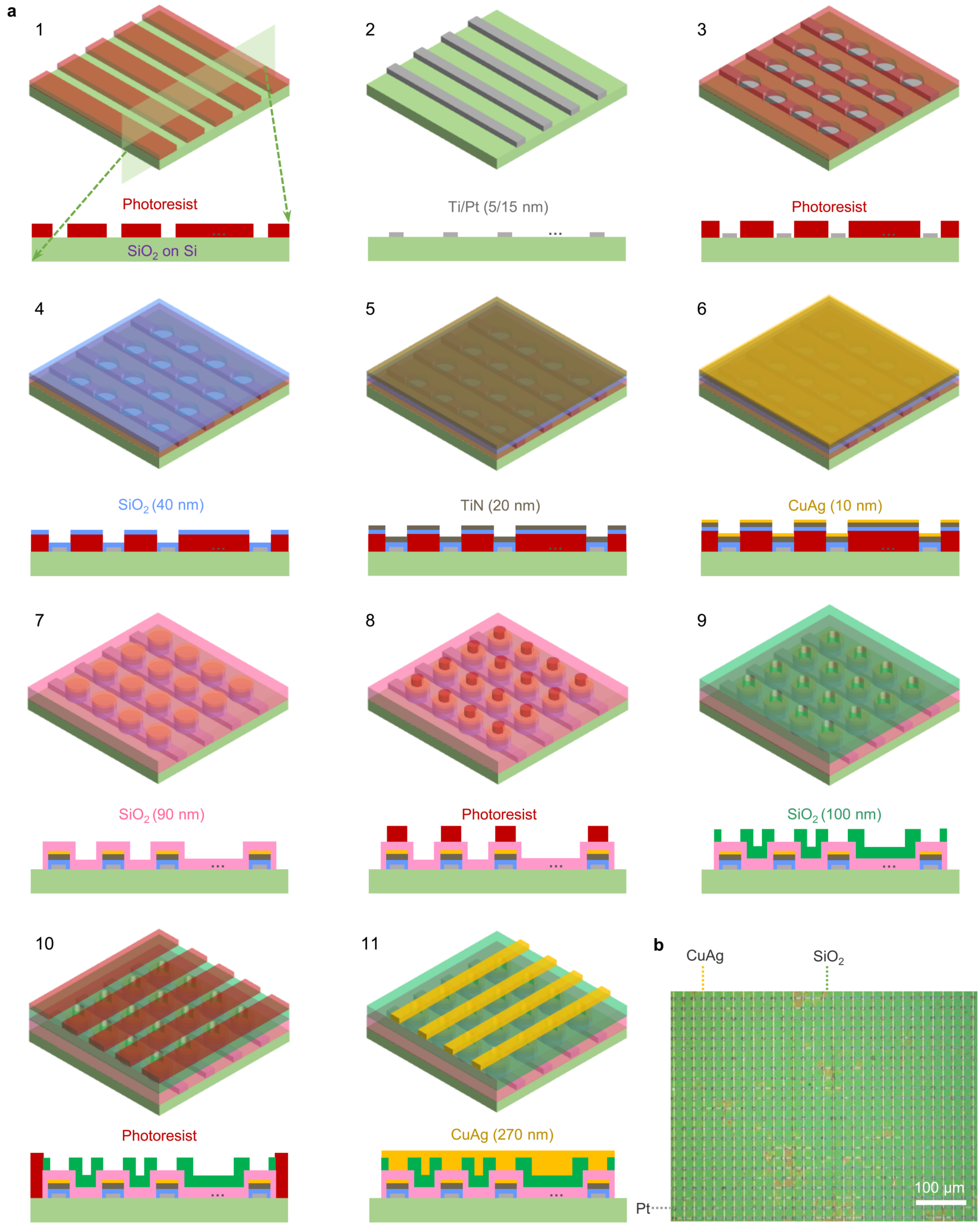

Supplementary Figure 9. A demonstration of 3D stacking 1S1R. a, Schematic top views and side cross-section views of the manufacturing processes of the 1S1R array (some lift-off steps are omitted). After photolithographic patterning (step **1**), electron beam evaporation (step **2**) and lift-off, 64 rows Ti (5 nm)/Pt (15 nm) BE with a linewidth of 2 μm are patterned. Then 64 × 64 sets of circular patterns with 5 μm diameter are obtained by photolithography (step **3**). In steps **4**–**6**, SiO_2, TiN, and CuAg are deposited (thicknesses of 40, 20, and 10 nm, respectively), yielding cylinders with diameter of 5 μm after lift-off. The SiO_2 in step **7** is used for the dielectric layer of the selector (thickness = 90 nm), while the SiO_2 (thickness = 100 nm) obtained after steps **8** (photolithography) and **9** (electron beam evaporation) is used to encapsulate the area beyond the cross-point and prevent contact between the TE (CuAg, step **11**) and the intermediate electrode (TiN and CuAg, steps **5** and **6**). The step **9** will leave holes with a diameter of 2 μm. Finally, after steps **10** (photolithography), **11** (co-sputtering) and lift-off, 64 columns CuAg electrodes (thickness = 270 nm) with a linewidth of 2 μm are patterned. At this point, the CuAg TE make contact with the 90 nm SiO_2 layer (step **7**) through the holes left by the 100 nm SiO_2 (step **9**). **b**, A top view of the 64 × 64 1S1R array, the electrode linewidths of BE and TE are 2 μm.

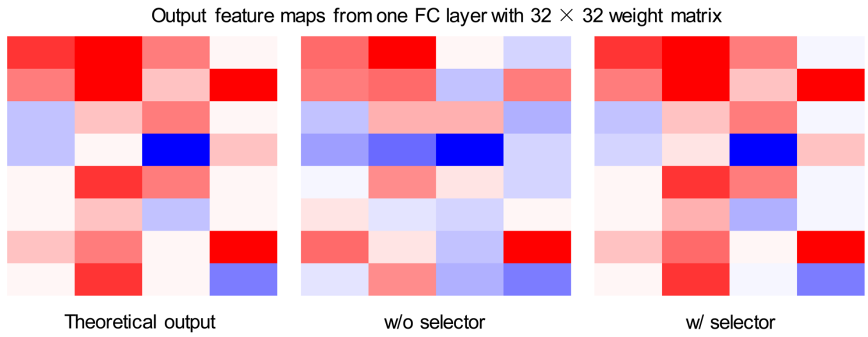

Supplementary Figure 10. Output feature map obtained by VMM simulation using one fully connected (FC) layer with 32 × 32 weight matrix for the theoretical output (left), without selector (middle), and with selector (right), respectively.

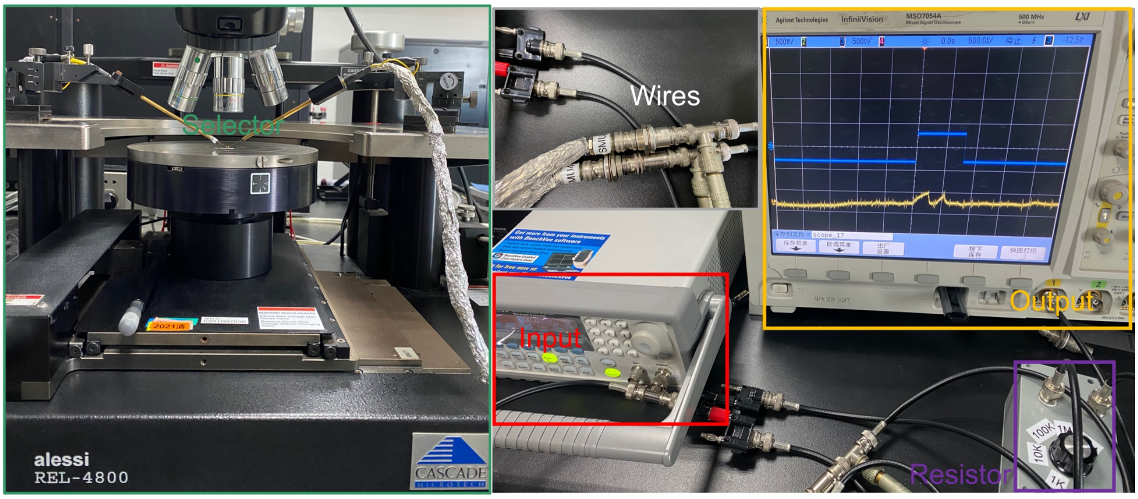

Supplementary Figure 11. Experimental setup for the waveform measurements of selector-based LIF neuron, including a probe station, an Agilent oscilloscope, a Keysight source meter and other components/wiring.

Supplementary References

1. Elton, L. & Jackson, D. F. X-ray diffraction and the Bragg law. *Am. J. Phys.* **34**, 1036–1038 (1966).
2. Holzwarth, U. & Gibson, N. The Scherrer equation versus the'Debye-Scherrer equation'. *Nat. Nanotechnol.* **6**, 534–534 (2011).
3. Wang, Z. *et al.* Memristors with diffusive dynamics as synaptic emulators for neuromorphic computing. *Nat. Mater.* **16**, 101–108 (2017).
4. Blöchl, P. E. Projector augmented-wave method. *Phys. Rev. B* **50**, 17953–17979 (1994).
5. Kresse, G. & Joubert, D. From ultrasoft pseudopotentials to the projector augmented-wave method. *Phys. Rev. B* **59**, 1758–1775 (1999).
6. Perdew, J. P., Burke, K. & Ernzerhof, M. Generalized gradient approximation made simple. *Phys. Rev. Lett.* **77**, 3865–3868 (1996).
7. Kresse, G. & Hafner, J. Ab initio molecular dynamics for liquid metals. *Phys. Rev. B* **47**, 558–561 (1993).
8. Kresse, G. & Hafner, J. Ab initio molecular-dynamics simulation of the liquid-metal–amorphous-semiconductor transition in germanium. *Phys. Rev. B* **49**, 14251–14269 (1994).
9. Kresse, G. & Furthmüller, J. Efficiency of ab-initio total energy calculations for metals and semiconductors using a plane-wave basis set. *Comput. Mater. Sci.* **6**, 15–50 (1996).
10. Kresse, G. & Furthmüller, J. Efficient iterative schemes for ab initio total-energy calculations using a plane-wave basis set. *Phys. Rev. B* **54**, 11169–11186 (1996).
11. Sheppard, D., Xiao, P., Chemelewski, W., Johnson, D. D. & Henkelman, G. A generalized solid-state nudged elastic band method. *J. Chem. Phys.* **136**, 074103 (2012).
12. Henkelman, G., Uberuaga, B. P. & Jónsson, H. A climbing image nudged elastic band method for finding saddle points and minimum energy paths. *J. Chem. Phys.* **113**, 9901–9904 (2000).

13. Henkelman, G. & Jónsson, H. Improved tangent estimate in the nudged elastic band method for finding minimum energy paths and saddle points. *J. Chem. Phys.* **113**, 9978–9985 (2000).

14. Xue, K.-H. *et al.* Theoretical investigation of the Ag filament morphology in conductive bridge random access memories. *J. Appl. Phys.* **124**, 152125 (2018).

15. Liu, Q. *et al.* Controllable growth of nanoscale conductive filaments in solid-electrolyte-based ReRAM by using a metal nanocrystal covered bottom electrode. *ACS Nano* **4**, 6162–6168 (2010).

16. Barshilia, H. C. & Rajam, K. Raman spectroscopy studies on the thermal stability of TiN, CrN, TiAlN coatings and nanolayered TiN/CrN, TiAlN/CrN multilayer coatings. *J. Mater. Res.* **19**, 3196–3205 (2004).

17. Yang, X. *et al.* Dual-function electron-conductive, hole-blocking titanium nitride contacts for efficient silicon solar cells. *Joule* **3**, 1314–1327 (2019).

18. Cheng, Y., Tay, B., Lau, S. P., Kupfer, H. & Richter, F. Substrate bias dependence of Raman spectra for TiN films deposited by filtered cathodic vacuum arc. *J. Appl. Phys.* **92**, 1845–1849 (2002).